First-principles analysis of the effect of magnetic states on the oxygen vacancy formation energy in doped $La_{0.5}Sr_{0.5}CoO_3$ perovskite

Wei Wei,[*] Florian Fuchs,[†] Andreas Zienert, Xiao Hu, and Jörg Schuster
Center for Micro and Nano Technologies, Chemnitz University of Technology, 09107 Chemnitz, Germany and Fraunhofer Institute for Electronic Nano Systems, 09126 Chemnitz, Germany

(Received 22 July 2025; accepted 23 July 2026; published 18 August 2026)

Oxygen vacancies are critical for determining the electrochemical performance of fast oxygen ion conductors. The perovskite $La_{0.5}Sr_{0.5}CoO_3$, known for its excellent mixed ionic-electronic conduction, has attracted significant attention due to its favorable vacancy characteristics. In this study, we employ first-principles calculations to systematically investigate the impact of 3*d* transition-metal doping on the oxygen vacancy formation energies in the perovskite. Two magnetic states, namely the ferromagnetic and paramagnetic states, are considered in our models to capture the influence of magnetic effects on oxygen vacancy energetics. Our results reveal that the oxygen vacancy formation energies are strongly dependent on both the dopant species and the magnetic state. Notably, the magnetic states alter the vacancy formation energy in a dopant-specific manner due to double exchange interactions, indicating that relying solely on the ferromagnetic ground state may result in misleading trends in doping behavior. These findings emphasize the importance of accounting for magnetic effects when investigating oxygen vacancy properties in perovskite oxides.

DOI: 10.1103/6ycm-9ttt

I. INTRODUCTION

Defect-driven transport phenomena are fundamental to the operation of fast ion-conducting solid electrodes and electrolytes [1]. During operation, intrinsic or extrinsic defects serve as the primary pathways for ionic migration. Among these defects, the critical role of oxygen vacancies extends to a broad class of fast-ion conductors, where their presence and mobility directly impact the efficiency of oxygen-ion transport [2,3]. Materials that accommodate high concentrations of oxygen vacancies, such as fluorite and perovskite crystals, often exhibit enhanced ionic conductivity and redox behavior, which are vital for applications including solid oxide fuel cells (SOFCs) and oxygen separation membranes [4,5]. Within this context, perovskite crystals have garnered significant attention due to their tunable defect chemistry and fast oxygen-ion conduction.

The perovskite framework, namely the compound of ABO_3, exhibits enhanced flexibility among the family of metal oxides [6]. This superior adaptability facilitates a broader range of ionic substitutions and the accommodation of various structural defects. Among them, the cobalt-based perovskites are a prominent category due to their exceptional oxygen diffusivity and oxygen surface exchange coefficient [7]. Various studies of A-position and B-position occupants have been added to such materials to accommodate a wide range of operating conditions. The inherent tunability of their B-site cation allows for precise engineering of oxygen vacancy formation and ionic transport properties [8]. For instance, partial substitution of Co with other transition-metal (TM) elements has been extensively explored to enhance stability under operational conditions or optimize ionic conductivity [9].

Despite these advances, open questions remain concerning the interplay between dopant chemistry and oxygen vacancy behavior, particularly under different manufacturing methods. Previous experimental studies have developed strategies such as nanostructuring, surface modification, and composite designs to improve the oxygen reduction reaction activity and durability of perovskite cathodes [10,11]. However, these methods frequently depend on the synergistic effect of multiple factors, resulting in the potential for contradictory outcomes for the same dopant elements. For example, Cheng *et al.* reported that Fe doping increases the concentration of lattice oxygen vacancies, thereby enhancing the performance of $La_{1-x}Sr_xCoO_{3-\delta}$ [12]. In contrast, Mantzavinos *et al.* observed that increasing Fe content leads to a decrease in oxygen vacancy concentration [13]. Consequently, theoretical calculations have been sought to elucidate the intrinsic effect of doping elements on the nature of oxygen vacancies in the perovskite [14].

Extensive theoretical studies have been conducted to investigate oxygen vacancy formation in cobalt-based perovskites [14–16]. However, these studies often focus on single-element doping effects and assume an idealized ferromagnetic (FM) ground state, neglecting the paramagnetic (PM) states that prevail at elevated temperatures during device operation [11]. This oversight limits the predictive accuracy and rationality of computational models. For instance, Jia *et al.* demonstrated

[*]Contact author: wei36188@gmail.com
[†]Contact author: florian.fuchs@enas.fraunhofer.de

Published by the American Physical Society under the terms of the Creative Commons Attribution 4.0 International license. Further distribution of this work must maintain attribution to the author(s) and the published article's title, journal citation, and DOI.

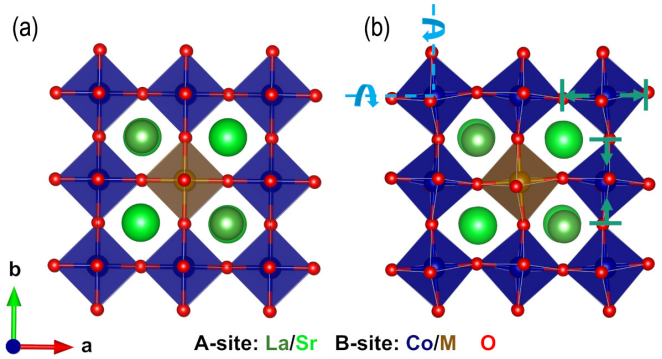


FIG. 1. Atomic structures of doped LSC. (a) The ordered perovskite structure with the dopant M substituting for Co at a B site. (b) The distorted structure induced by the J-T effect and A-site mismatch. The light blue arrows indicate the rotation of the B-O octahedra, while the dark green arrows indicate the bond length stretch by the J-T effect. La/Sr atoms are shown in dark/light green, Co atoms in blue, O atoms in red, and the dopant site by M is marked in dark gold.

that Fe doping of cobalt-based perovskites decreases oxygen vacancy formation energy in the PM state [17]. This variation underscores the necessity of incorporating both magnetic states into theoretical investigations to accurately predict dopants behavior in operational environments.

In this work, we systematically investigate the impact of substituting Co with Mn, Fe, Ni, and Cu on the energetics of oxygen vacancy formation in $La_{0.5}Sr_{0.5}CoO_3$ (LSC), considering both FM and PM states. Using density functional theory (DFT), we evaluate the interplay among dopant electronic configurations, magnetic order/disorder, and oxygen vacancy stability. These findings provide key insights for designing next-generation perovskite SOFC cathodes with tailored oxygen vacancy concentrations and enhanced electrochemical performance.

The paper is organized as follows. In Sec. II we introduce the computational setup and the definition of the formation energy of oxygen vacancies in LSC. In Sec. III, we present the results on stability of oxygen vacancies by different magnetic states, and its influence on the electronic structure. In Sec. IV, we discuss our results in view of other findings in the literature, and we summarize and conclude in Sec. V.

II. THEORETICAL APPROACH

A. Crystal structure of LSC

In earlier studies, the parent LSC phase was considered to adopt a cubic perovskite structure (space group $Pm\bar{3}m$) under operating conditions and room temperature [18,19]. The structure consists of corner-sharing $CoO_6^{2/3-}$ octahedra, with La^{3+} and Sr^{2+} ions randomly occupying the A site, creating a disordered cationic sublattice. Investigations on similar perovskites have further revealed that the energies associated with different La/Sr configurations are very close, allowing the use of isotropic supercells to reliably capture the average structural and electronic properties of these materials [20,21]. A perfect cubic model with an ordered La/Sr configuration is depicted in Fig. 1(a). The lattice constant of this cubic model is 3.85 Å by DFT, which is in agreement with the experimental values of 3.83–3.84 Å [22–24]. However, more recent studies indicate that under operating conditions, particularly in thin films, LSC does not maintain a perfect cubic symmetry but rather exhibits a pseudocubic structure characterized by distortions in the Co-O octahedra [15,25,26].

TABLE I. The oxidation and magnetic states of TM ions, as well as the magnetic state of the V_O.

Element	Oxidation	Magnetic moment	Magnetic moment shift by V_O
Mn	3+	3.1 μ_B (HS)	0 μ_B
Fe	3+	3.9 μ_B (HS)	−2 μ_B
Co	3+/4+	1.5/2.9 μ_B (IS)	−2 μ_B
Ni	2+	1.8 μ_B (HS)	0 μ_B
Cu	2+	−0.7 μ_B	0 μ_B

The pseudocubic structure of LSC with distorted Co-O octahedra can be mainly attributed to two reasons: bond length stretch and bond angle rotation. Stretching of bond lengths is primarily due to the Jahn-Teller (J-T) effect [27,28]. The J-T effect arises from electronic degeneracies in the Co d orbitals, which drive a spontaneous symmetry breaking in the CoO_6 octahedra to lower the energy of the system [29,30], while rotation of bond angles is mainly caused by differences in the ionic radii and charges in the crystal lattice, particularly between La and Sr ions. The effective ionic radii of La^{3+} and Sr^{2+} are 1.216 Å and 1.310 Å, respectively [31], and their differing charges result in distinct interactions with the surrounding ions. Such structural modifications yield the lattice constant to 3.87 Å, and have profound implications on the electronic structure and oxygen vacancy formation energetics, thereby influencing the electrochemical performance of the material [32]. Therefore, we have incorporated the structural distortion into our model, as illustrated in Fig. 1(b). The ground state of the LSC structure is optimized by the USPEX evolutionary algorithm [33] to escape local minima and thereby determine the global energy minimum of the system, see the energy of the candidate structures in Fig. S1 in the Supplemental Material [34].

In our models, we replace one of the Co atoms with the aforementioned TM elements. At 1/8 doping concentration, the lattice constant change slightly. The lattice constants of the Mn-, Fe-, Ni-, and Cu-doped systems are 3.87, 3.87, 3.88, and 3.88 Å, respectively. The calculations for each doped system are based on these lattice constants.

B. Magnetic order calculations

The magnetic properties of LSC are governed by the complex interplay between Co^{3+}/Co^{4+} spin states and oxygen vacancy distributions [35]. At temperatures lower than 250 K, LSC exhibits FM ordering due to double exchange between two Co ions through the intermediate shared O atom [18,19]. To identify the ground state of FM configuration, we calculate the spin states by initializing the magnetic moments of Co ions at all integer numbers between 0 and 5 μ_B. The calculations are also performed on the doped systems, and the results are shown together in Table I. In pristine LSC, Co ions are stable

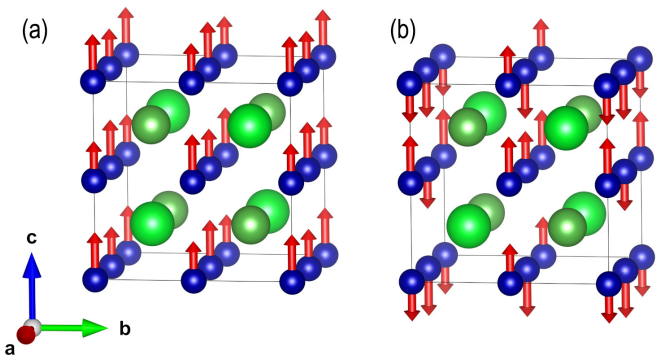


FIG. 2. Magnetic configurations of LSC: (a) the FM state, and (b) one of the PM state configurations. The magnetic moments of TM elements are represented by red arrows. To improve clarity, oxygen atoms are not shown.

in the intermediate spin (IS) state. In doped systems, Cu ions exhibit the opposite spin state to neighboring Co ions, while Mn, Fe, and Ni ions occupy the high-spin (HS) state. The calculated magnetic moments are less than the formally expected integer numbers due to delocalization and orbital hybridization effects occur in the electron cloud between atoms. The oxidation states of the TM ions are calculated using localized orbital bonding analysis [36] with the MULTIWFN code [37].

The ground state of the oxygen vacancy are also determined by comparing the energies of different spin states. We perform calculations for different spin states (integer number from –3 to $+3\,\mu_B$ to the total spin of pristine crystal) in the structure with a vacancy to determine the ground state. By subtracting the total spin of the pristine crystal from that of the vacancy-containing structure, we obtain the spin state of the O vacancy. In pristine and Fe-doped LSC, the most stable oxygen vacancy exhibits a magnetic moment of $-2\,\mu_B$, while in other doped systems, the magnetic moment does not change by the oxygen vacancy, as shown in Table I.

However, at most operating temperatures, thermal fluctuations disrupt the long-range FM order, leading to a PM state with short-range spin correlations [35]. Simulating the exact noncollinear magnetic configurations in the PM state is computationally expensive due to the size of the supercell and the need for extensive statistical sampling. Instead, we employ the magnetic sampling method (MSM) [38], which simulates PM states using the average of a certain mount of collinear magnetic configurations, as shown in Fig. 2. In each of the samples, the total magnetic moment is control to $0\,\mu_B$. The MSM approach has been validated against more rigorous methods (e.g., DLM-CPA) for transition-metal oxides, yielding comparable accuracy in predicting magnetic and electronic properties [38].

Understanding the MSM can be started from the classical Heisenberg model with the Hamiltonian:

$$H_{\text{mag}} = -\sum_{i\neq j} J_{ij}\vec{S}_i \cdot \vec{S}_j, \tag{1}$$

where J_{ij} represents the exchange interaction between i and j ions. $\vec{S}_i$ and $\vec{S}_j$ are the spin vectors, which are normalized to 1 to ensure that parameters are in units of energy. To achieve an ideal random distribution of magnetic spins, with aiming to simulate PM states corresponding in the Heisenberg model, it is necessary to ensure the vanishing of all average spin correlation:

$$-\sum_{i\neq j} \vec{S}_i \cdot \vec{S}_j = 0. \tag{2}$$

The directions (up and down) of magnetic moments of the TM ions are chosen using a random number generator. A single configuration will not result in 0, but the parallel ($\vec{S}_i \cdot \vec{S}_j = +1$) and antiparallel ($\vec{S}_i \cdot \vec{S}_j = -1$) pairs formed after multiple random magnetic samplings will cancel each other, consequently resulting in 0.

In this work, the MSM implementation involves generating 20 distinct collinear spin configurations for our models. This approach captures the essential physics of the PM state while maintaining computational feasibility, as demonstrated by its successful application to similar transition-metal oxides systems [39–41].

C. Computational details

The calculations are carried out with the Vienna *ab initio* simulation package (VASP) [42] employing projector-augmented waves [43] and the GGA-PBE [44] functional. Spin polarization is enabled for calculations involving magnetic systems. The following orbitals are taken as valence states in our calculations: 5*s*, 5*p*, and 6*s* orbitals of La, the 4*s*, 4*p*, and 5*s* orbitals of Sr, the 3*s*, 3*p*, 3*d*, and 4*s* orbitals of TM elements, and the 2*s* and 2*p* orbitals of O. To avoid the self-interaction errors that occur in the standard DFT for strongly correlated electronic systems, we employ the DFT + U method [45] accounting for the on-site Coulomb interaction in the localized *d* orbital.

In our calculations, an energy cutoff of 600 eV is used for the plane-wave basis. The threshold of SCF convergence and force on atoms for all structures are converged within 1×10^{-5} eV and 5×10^{-2} eV/Å, respectively. The Brillouin-zone integrals are sampled by $4 \times 4 \times 4$ Γ-centered k-point grids with a Gaussian smearing of 1×10^{-3} eV for the $2 \times 2 \times 2$ supercell models containing 40 atoms with composition $La_{0.5}Sr_{0.5}Co_{0.875}M_{0.125}O_3$ (M = Mn, Fe, Co, Ni, Cu). The specific U values employed are 4.0 eV for Mn, Cu, and Fe, 3.3 eV for Co, and 6.4 eV for Ni [46]. The employed parameters mentioned above have been tested and selected, see Figs. S2–S5 in the Supplemental Material [34].

Defect formation energies of TM dopants located at B sites in the perovskite crystal are calculated as

$$E_{\text{TM}}^{\text{doping}} = \frac{E_{(\text{La/Sr})\text{Co}_{1-y}\text{M}_y\text{O}_3} - E_{\text{LSC}}^{\text{bulk}} - y\left(E_{\text{M}}^{\text{metal}} - E_{\text{Co}}^{\text{metal}}\right)}{y}, \tag{3}$$

where $E_{(\text{La/Sr})\text{Co}_{1-y}\text{M}_y\text{O}_3}$ is the total energy per formula unit of the doped perovskite crystal, $E_{\text{LSC}}^{\text{bulk}}$ is the energy per formula unit of the pure LSC reference crystal, $E_{\text{M}}^{\text{metal}}$ and $E_{\text{Co}}^{\text{metal}}$ are the energy per atom in the most stable phase of the elemental metals, and y is the proportion of dopant per formula unit of the perovskite crystal.

Similarly, the formation energy of an oxygen vacancy in the perovskite crystal is calculated as

$$E_V^O = E_{sys}^{vac} - E_{sys}^{bulk} + \tfrac{1}{2}E_{O_2}, \quad (4)$$

where E_{sys}^{vac} is the total energy of the (doped or nondoped) perovskite crystal with an oxygen vacancy, E_{sys}^{bulk} is the total energy of the same crystal without oxygen vacancies, and E_{O_2} is the energy of an oxygen molecule. In our calculations, we consider a single oxygen vacancy by removing one O atom from a total of 24 O atoms in our model.

III. RESULTS

A. Structural distortion of LSC

To elucidate the energy landscape associated with distortions of CoO_6 octahedra in LSC, we investigated the relative energy as a function of the B-O-B bond angle distortion. As demonstrated in Fig. 3(a), we compared the potential energy surface of two distinct magnetic configurations: FM and PM states. In our results, all energies are referenced to the lowest energy point in the FM configuration, which is set to 0 eV. The energy profiles exhibit a characteristic double-well potential, with minima corresponding to distorted structures and a local energy maximum at the undistorted cubic phase (0° distortion). Deviations from 0° represent increasing distortion, with positive and negative angles indicating different distortion directions.

The stability of different magnetic configurations varies with structural distortions. The FM configuration exhibits its minimum energy at a distorted angle of ±15°. While, the PM configuration shows a higher energy minimum at a similar distortion angle, which is ±16°, with an energy difference of 0.08 eV per formula unit relative to the FM state. At the perfect crystal at 0°, the PM state is slightly more stable than the FM state, with the PM energy being 0.01 eV lower than that of the FM configuration. While in the 0° J-T distorted structure, the energies of both magnetic states show a clear decrease, with the FM state exhibiting a more stabilization of approximately 0.07 eV compared to the PM state. These observations indicate that while both FM and PM states favor distorted structures over the cubic phase, the FM state stabilizes the distorted phases more effectively.

Then, in Fig. 3(b), we compare the DOS plots for the Co^{4+} 3*d* in the LSC. The *d* band is shown in e_g and t_{2g} symmetries. We can clearly see that, compared to the nondistorted structure, the distorted structure exhibits splitting in both the e_g and t_{2g} orbitals, which is consistent with the classical J-T effect [27]. Additionally, as structural distortion increases, the *d* orbitals become more delocalized, and the band center shifts to the left, indicating lower energy.

To further investigate the role of structural distortion in the presence of oxygen vacancies, we analyze the total energy of vacancy-containing systems as a function of B-O-B bond angle distortion, as shown in Fig. 4. We compute the total energy in three distinct ways: first, the ordered structure without relaxation (space group *Cmm*2), second, the ordered structure with relaxation (space group *Cmm*2), and third, the distorted structure with relaxation in no symmetry (space group *P*1). In the three structures, the distortion increases from the first to the last. The E_V^O for the structures are also provided. For the distorted structure, the energy is approximately 1.2 eV. On the other hand, when using the pristine ordered structure (space group $Fm\bar{3}m$) as a reference, the energy in a symmetry-preserved system (space group *Cmm*2) is notably reduced to around 0.5 eV, demonstrating the strong influence of structural distortions on defect energetics. Furthermore, a nonrelaxed ordered structure yields the energy to approximately 1.6 eV,

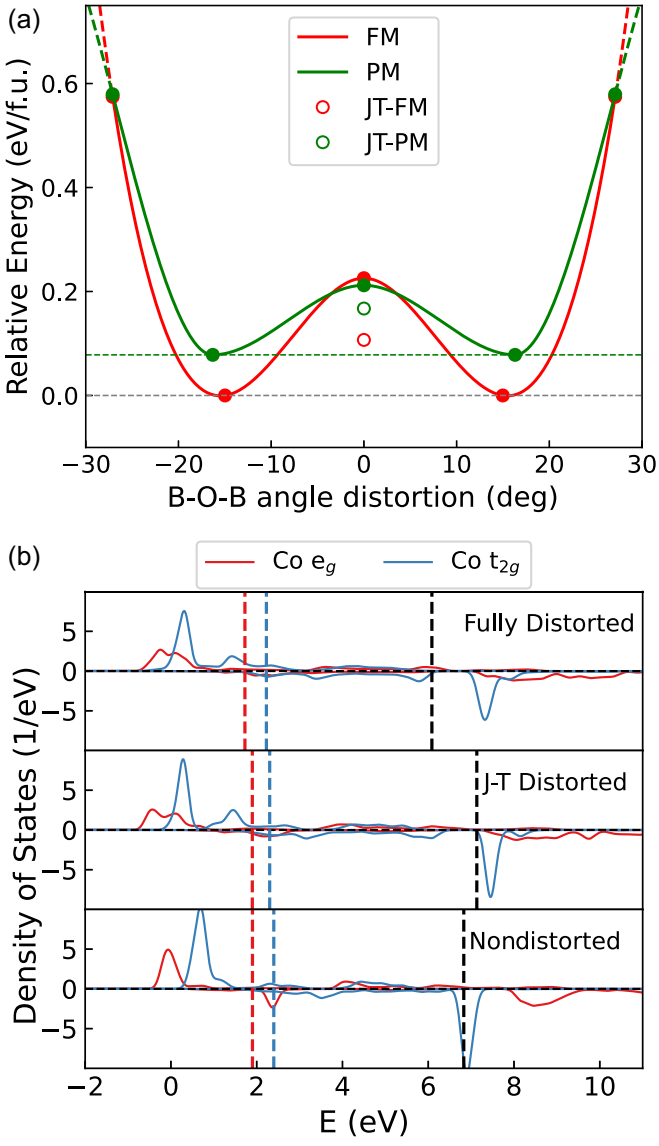


FIG. 3. (a) Relative energy per formula unit as a function of B-O-B angle distortion in LSC for FM (red) and PM (green) configurations. The energy decrease by the J-T effect is also shown by hollow circles. All energies are referenced to the lowest energy point in the FM configuration, marked as 0 eV on the vertical axis. (b) The comparison of the d-orbitals (by e_g and t_{2g} symmetry) DOS of a Co^{4+} ion in the fully distorted, J-T distorted, and not-distorted structures. The nondistorted structure corresponds to the local energy maximum of FM at 0°, while the fully distorted structure is the lowest energy configuration in FM. The band center of the e_g and t_{2g} orbitals are labeled in the dashed line by the same color, and the Fermi level is labeled by the black dashed lines.

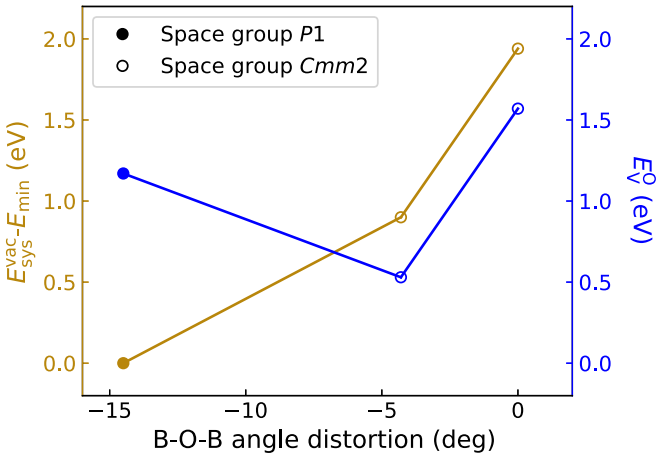


FIG. 4. Energy analysis of vacancy-containing LSC structures as a function of B-O-B angle distortion. The dark yellow curve represents the total system energy E_{sys}^{vac}, referenced to the lowest energy configuration E_{min}. The blue curve shows the oxygen vacancy formation energy E_V^O. The solid and open markers indicate different symmetry of the crystal.

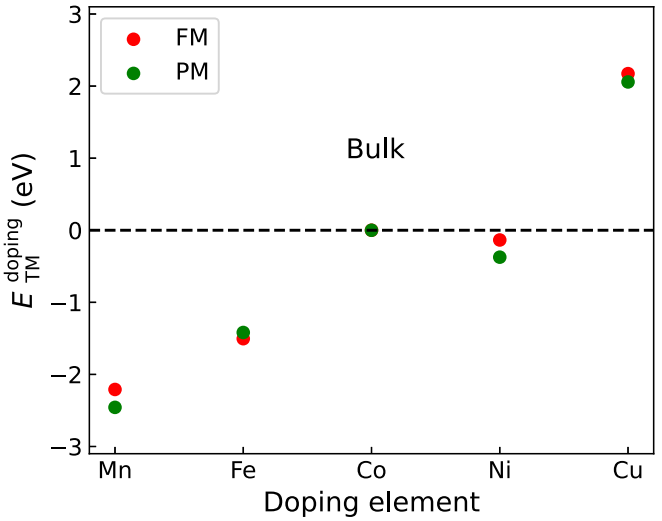


FIG. 5. Doping energy of pristine LSC with transition metal dopants (Mn, Fe, Ni, Cu) substituting a single Co atom. Red and green circles denote ferromagnetic (FM) and paramagnetic (PM) configurations, respectively. In both magnetic states, the formation energy of pure LSC, indicated by Co, was set to be zero as the reference.

which is 0.4 eV higher than the value obtained for the distorted system. To ensure that the vacancy formation energy and the doping energy are comparable in different systems, we uniformly employed fully distorted structures for all subsequent calculations.

B. Oxygen vacancies in doped LSC

In order to study the effects of dopant elements on the formation energy of oxygen vacancies, an initial investigation of the formation energy of substituting a single Co atom with TM dopants (Mn, Fe, Ni, Cu) in the pristine LSC crystal is conducted. We then calculate the formation energy of oxygen vacancies in the investigated material systems. In the bulk phase of metallic systems, the free electrons in the metallic system strongly shield the local net charge, rapidly neutralizing it. Consequently, we ignore the charge states, and treat all point defects as neutral.

Figure 5 illustrates the TM-doping energies under FM and PM states. A clear correlation is observed between the TM doping energy trends in FM state, suggesting that the stability of doped LSC is governed by the intrinsic oxidation energies of the dopants. This trend is similar to the reported oxide formation energies of the dopant elements [46]. Most of the doping energies in the PM state exhibit a slight reduction (0.1–0.3 eV) compared to those in the FM state across all dopants, the only outlier is Fe dopant, which increases the energy slightly. However, these differences do not alter the overall energetic trend. The consistent trend implies that magnetic ordering barely affects the relative stability of dopants.

We then investigate E_V^O in doped LSC depending on the magnetic states. Figure 6 compares E_V^O for first-nearest-neighbor (1NN) and second-nearest-neighbor (2NN) vacancy sites relative to the dopant site, respectively.

First, we investigate the effect of vacancy position on their formation energies. The doping elements affect not only the O atoms with which they form chemical bonds, but also the other O atoms by affecting the neighboring Co atoms. In the presence of TM dopants, differences in the formation energies of two different oxygen vacancy sites have been observed. These variations can even alter the relative stability (compare the E_V^O in pure LSC) of the vacancies. Therefore, it is essential to consider both vacancy sites to understand the dopant-induced effects on the stability of the vacancies.

Next, we compare the vacancy formation energy between the FM and PM state. The PM state lowers E_V^O (compared to FM) for both 1NN and 2NN sites in most of the situations, which suggests that the PM state weakens the strength of TM-O bonds. This weakening is most pronounced in the pure LSC, resulting in an energy difference of 0.6 eV (difference between the dashed lines in Fig. 6). For the dopants, this energy difference ranges from 0.2 eV to 0.6 eV in most cases, while the Cu doping remains unchanged at the 1NN vacancy site.

Vacancy positions and magnetic states together create even more complex variations in oxygen vacancy stability. For the 1NN vacancy, the Fe-doped FM state exhibits a higher vacancy formation energy compared to the LSC. However, this tendency is reversed at the 2NN site. In contrast, for the PM state, the Fe-doped system exhibits higher vacancy formation energies than the LSC for both vacancy positions. For Ni and Cu doping, the stability of 1NN vacancy has also a noticeable change between the magnetic states. The energies in the FM state are lower than that in the LSC, while in the PM state they are always higher than its formation energy in the LSC. Consequently, the energy change induced by the PM magnetic state qualitatively affects stability of the oxygen vacancy in the doped system.

To further elucidate the interplay between defects and magnetic states, Fig. 7 quantifies the energy difference between the two magnetic states ($\Delta E_{\text{FM-PM}}$) for the crystals with and without oxygen vacancy. The results demonstrate an absence of regularity in the apparent changes in $\Delta E_{\text{FM-PM}}$.

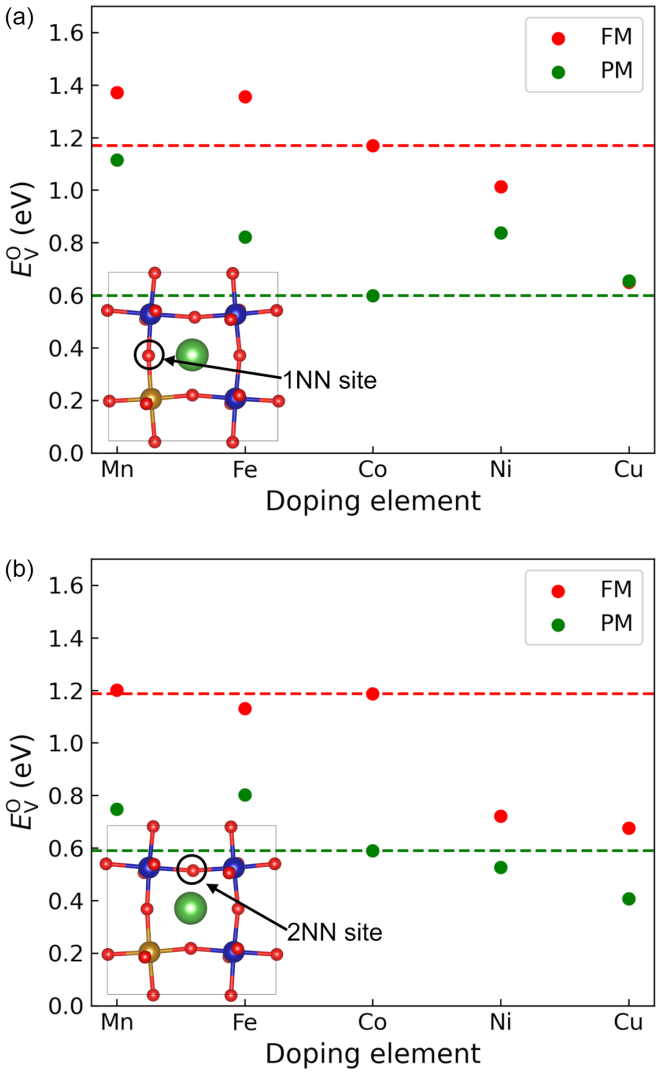


FIG. 6. Oxygen vacancy formation energy (a) at the 1NN and (b) at the 2NN sites of the doped LSC. FM and PM configurations are shown in red and green, respectively. For better comparison, the dashed lines mark E_V^O for the Co.

Specifically, the introduction of an oxygen vacancy alters $\Delta E_{\text{FM-PM}}$ in a dopant-dependent manner, suggesting that local structural and electronic rearrangements around the vacancy site significantly influence spin alignment preferences. The most pronounced change in $\Delta E_{\text{FM-PM}}$ due to oxygen vacancy formation is observed in pristine LSC, where the energy difference decreases by approximately 0.6 eV. The Fe-doped system show a similar decrease, by around 0.5 eV. Mn- and Ni-doped systems exhibit moderate decreases in the range of 0.3–0.2 eV. On the other hand, for Cu doping, the energy difference remains unchanged, indicating a weaker dependency between defect formation and magnetic stability in the system.

The results of this section illustrate the interplay among doping chemistry, oxygen vacancy defects, and magnetic order. However, these relationships do not exhibit an obvious trend. In particular, while our aim is to qualitatively elucidate the relationship between oxygen vacancy formation energy and magnetic order, significant variations are observed across

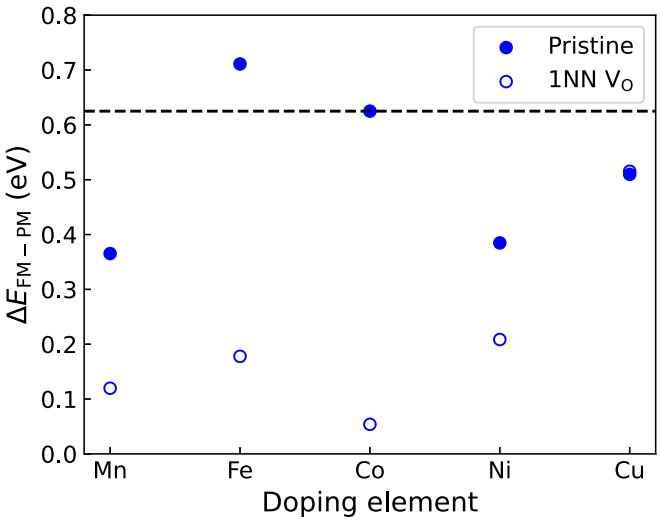


FIG. 7. Energy difference between PM and FM states ($\Delta E_{\text{FM-PM}}$) for pristine crystals and crystals with 1NN V_O, denoted as solid and open markers, respectively.

different compositional systems. Consequently, our calculations indicate it is necessary to investigate the electronic structure of the systems.

C. Electronic structure analysis

In order to assess the doping-induced modifications in the electronic structure of LSC, we conduct a comparative analysis of the projected density of states (pDOS) for the doped crystals. The pDOS of crystals without V_O are compared between the FM and PM states. For the sake of clarity, the contributions from La and Sr elements had been omitted from the figures.

Figure 8 illustrates the detailed information of the pDOS. The band center, as the effective electronic descriptor, is also labeled in the figure. The band center is defined as the energy-weighted average of the orbital, i.e., $\varepsilon_{\text{center}} = \frac{\int E \cdot D(E)\, dE}{\int D(E)\, dE}$ [47]. We only consider the p orbital of O at 1NN and 2NN sites, and the d orbital of TM elements (including Co) connected to these O sites. The energy difference between the center of the O $2p$ band and TM $3d$ band (ΔE_{cen}) is affected by the dopants and the magnetic states. For the FM state, Fe dopant maintain a similar ΔE_{cen} to LSC, while the Mn, Ni, and Cu dopants expand it compared to LSC by 0.37, 0.76, and 0.50 eV, respectively. On the other hand, in the PM state, Mn and Ni dopants show a similar ΔE_{cen} to LSC, while the Fe and Cu dopants decreases the ΔE_{cen} around 0.25 eV.

Furthermore, the change in ΔE_{cen} between the two magnetic states is also related to the type of dopants. Specifically, as the magnetic state transitions from FM to PM state, the ΔE_{cen} increases by 0.73 eV within a pure LSC crystal. The increases for Mn and Fe dopants are less than that for LSC, with 0.35 and 0.39 eV, respectively. Oppositely, the Ni and Cu dopants exhibit a slightly negative change with around –0.05 eV.

In summary, our pDOS analysis reveals that, while the overall energy landscapes of the TM $3d$ and O $2p$ states

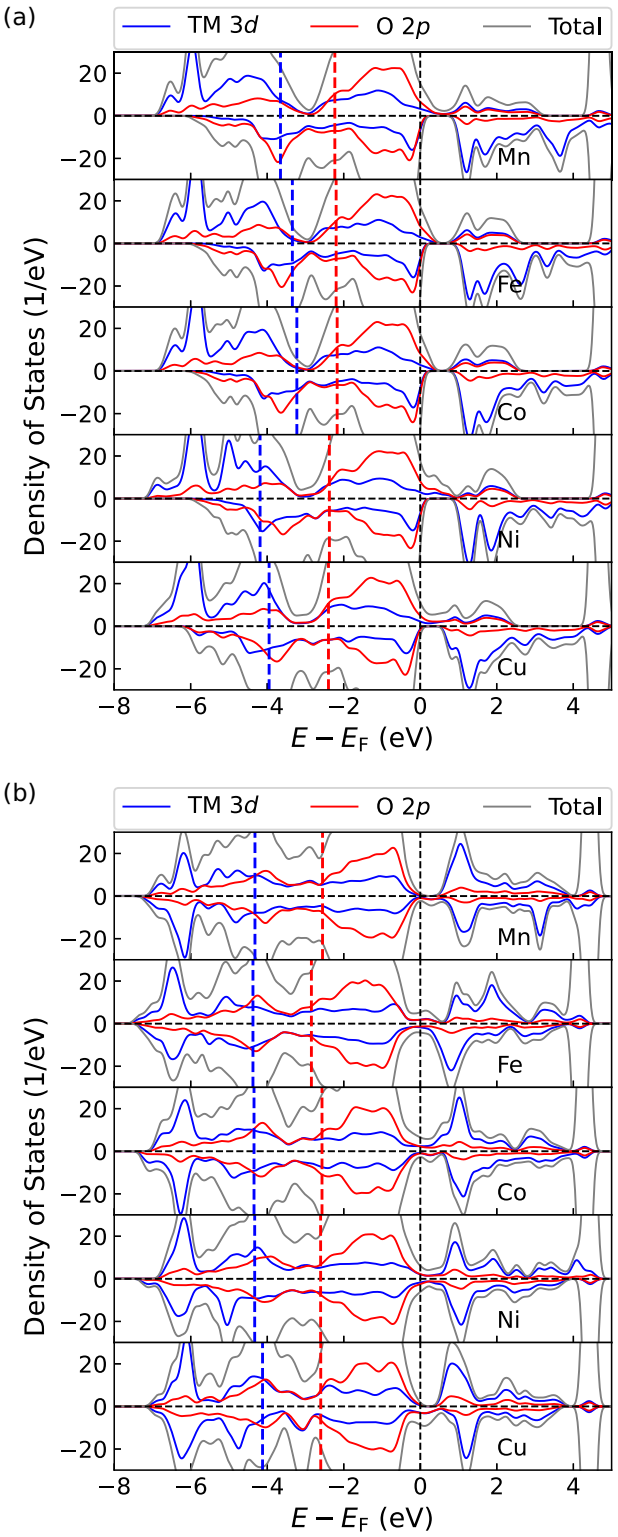


FIG. 8. Projected density of states for doped LSC of (a) the FM state and (b) the PM state. Each panel displays the TM 3*d* orbital (blue), the O 2*p* orbital (red), and the total density of states (gray), with energies referenced to the Fermi level (E_F). Spin-up and spin-down data are shown in each top and bottom panel, respectively. Vertical dashed lines denote the band centers of the occupied O 2*p* (red) and TM 3*d* (blue) states

remain qualitatively similar across all dopants, the band centers exhibit modifications that are dopant and magnetic state dependent. These results underscore the complex interplay between dopant chemistry and magnetic states in modulating the electronic structure of LSC.

IV. DISCUSSION

In this study, we presented the critical role of structural distortions in stabilizing the LSC system and modulating the formation energy of oxygen vacancies. Our findings are consistent with previous studies that have highlighted the significance of J-T distortions and octahedral tilting in transition-metal oxides [28,48]. Specifically, we observe that the cubic phase of LSC corresponds to a local energy maximum due to its inherent instability, whereas distorted structures are energetically favored, as illustrated in Fig. 3. This behavior is well documented in perovskite oxides, where cooperative J-T distortions lower the total energy and enhance the structural stability [49].

The comparison between the FM and PM states under the conditions of structural distortion further reveals intriguing stability trends. While both FM and PM states exhibit a preference for distorted structures over the ordered cubic phase, the FM state stabilizes the distorted structures more effectively. This observation is supported by prior theoretical investigations of transition metal perovskites, which indicate that magnetic ordering can influence the energy landscape by coupling to structural distortions [28,50]. Furthermore, the stability of the magnetic state is found to be contingent upon the distortion angles, suggesting a sensitivity of the magnetic state to the structural parameters. This sensitivity of the magnetic state to structural distortions is further substantiated by Woicik *et al*., who observed a change in the Curie temperature of LSC films under different strains [24].

Doping the 3*d* elements into LSC moderately changed the energy difference between the FM and PM states, without altering the ground magnetic state, which is a situation different to half-doped perovskite manganates. In the paramagnetic phase of half-doped manganates, electrons are localized at specific lattice sites, the material thus behaves as an insulator due to strong thermal fluctuations and Jahn-Teller distortion [51]. Some of the half-doped manganates discussed in the literature are located at phase transition critical points in the phase diagram; therefore, even a small amount of doping can trigger a phase transition, leading to the disruption of long-range electronic order. The phase transition points of half-doped cobaltite are also affected by dopants; however, the perovskite cobaltite we selected behaves as a conductor in both the FM and PM states, and the component we choose is far to the phase transition point. Therefore, the significant ground-state change observed in half-doped manganates does not occur in the LSC we selected.

E_V^O are also sensitive to the magnetic states. The difference of E_V^O between the two magnetic states can be qualitatively explained by the double exchange interaction. The O atom between the two TM atoms is suggested to act as a bridge for double exchange in a FM perovskite oxide [52]. The presence of V_O diminishes the bridge, thereby increasing the energy of the entire system. Consequently, the E_V^O is expected to be

higher in the FM state compared to the PM state. However, as illustrated in Fig. 6, the E_V^O in FM and PM for Cu dopant is comparable, suggesting that Cu interrupt the double exchange before the presence of V_O. A similar phenomenon was reported by Mizokawa *et al*. [28], who indicated that the low-spin Cu in perovskites weaken the double exchange, which in turn destabilizes spin ordering. We include the spin orbital coupling (SOC) in the calculations for the pristine LSC and Cu-doped systems, as shown in Fig. S4 in the Supplemental Material [34], and found the SOC effect will not influence the energy trend.

The hypothesis of defect effects on the double exchange mechanism can also provide a qualitative framework for understanding their influence on the magnetic ordering temperature in LSC. Experimental studies by Baskar *et al.* [35] have shown that the presence of oxygen vacancies in LSC leads to a reduction in the magnetic ordering temperature compared to the pristine crystal. This observed decrease can be attributed to a reduction in the energy difference between the PM and FM states, a trend consistent with the results presented in Fig. 7 (Co, Mn, and Fe). Specifically, the suppression of the double exchange mechanism, caused by oxygen vacancies, decreases the relative stability of the ferromagnetic state, thereby lowering the magnetic ordering temperature. In contrast, for low-spin Cu dopant, the presence or absence of V_O has little effect on the relative stability of the two magnetic states in the doped LSC. In this case, the roles of oxygen vacancies and low-spin dopants in hindering the double exchange interaction are consistent.

To understand the different trends of double exchange interactions under various doping elements, we analyzed the electronic structure. The double exchange interaction exerts a significant influence on the distribution of electrons [53,54], and this phenomenon can be observed in the pDOS. Stronger double exchange increases the degree of orbital overlap and the strength of chemical bond [55], which in turn affects the corresponding band center distances. In the energy range under consideration, the density of states is predominantly governed by contributions from the B-site TM 3*d* orbitals (including both t_{2g} and e_g components) and O 2*p* orbitals. The occupied state centers of the O 2*p* and TM 3*d* bands are labeled in Fig. 8. In this figure, we provide data for two magnetic states, FM and PM, for comparison. Note that the band center is calculated under the conditions of pristine crystals without V_O. We expect to correlate the variations between them with the trends of E_V^O in different doped systems.

Figure 9 illustrates the relationship between the shift of ΔE_{cen} and the shift of E_V^O. These shifts arise from the difference between FM and PM states (FM minus PM). The band center takes into account the combined effects of the properties of the elements themselves and the double exchange interactions. We refrain to label the elements in this figure, as all systems should conform to our hypothesis. All the data points form an approximate linear relationship.

This linear relationship confirms our earlier hypothesis that defects influence double exchange interactions. The doping elements partially obstruct the double exchange interaction, whereas the presence of V_O is likely to completely obstruct them. When the doping elements fully obstruct the double exchange interactions, there is little change in the shift of

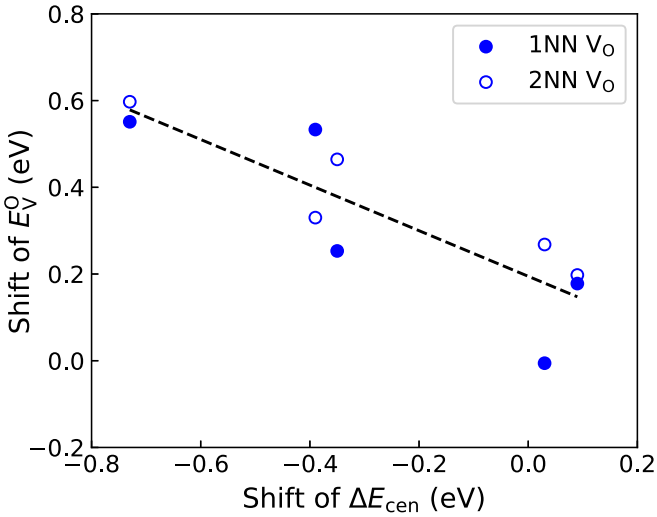


FIG. 9. Scatter plot of the energy difference between O 2*p* and TM 3*d* band centers versus the energy difference between FM and PM states in doped LSC. Solid and open blue circles denote the two different oxygen vacancies. The dashed line is the linear fitting of all data points.

E_V^O, corresponding to the right part of the line. Conversely, when the doping elements do not fully hinder double exchange interactions, the V_O takes responsibility for hindering the remaining double exchange interactions, thus increasing E_V^O, which corresponds to the left part of the line. Therefore, the influence of doping elements on E_V^O exhibits inconsistent trends under different magnetic states, and this inconsistency is determined by the varying degrees of hindrance that defects impose on double exchange interactions.

To further determine the role of double exchange interactions, we expanded the discussion on exchange interactions with orbital hybridization in an Co-O-TM system, and performed calculations of the effective exchange coefficient *J*. First, we analyzed the projected DOS for the TM and Co ions connected to the target O atom (at 1NN site) to examine the influence of orbital hybridization, as shown in Fig. 10. In pristine LSC and Fe-doped systems, the t_{2g} orbitals of the TM (including Co) and the *p* orbitals of O exhibit coincident peaks near the Fermi level, indicating a strong orbital hybridization driven by double exchange. The strong-coupling double exchange mechanism mediated by t_{2g} electrons is also found in experiments [56]. In contrast, the hybridization is suppressed in the Mn-doped system, indicating that the double exchange interaction between Mn and Co is weaker than that in Co-O-Co and Fe-O-Co cases. The Cu and Ni doping exhibit a similar (or maybe a little weaker) hybridization without qualitative deviation from Mn doping, but the Ni-doped system displays a prominent spin-down localized peak at –4.3 eV, indicative of stronger superexchange interactions. The presence of two such spin-down peaks in the Cu-doped system suggests it possesses the strongest superexchange interaction among the studied cases.

Then, we calculated the exchange interactions between the two TM ions The competition between superexchange and double exchange is characterized by the exchange coupling constant *J*. Quantitative analyses of the magnetic states of

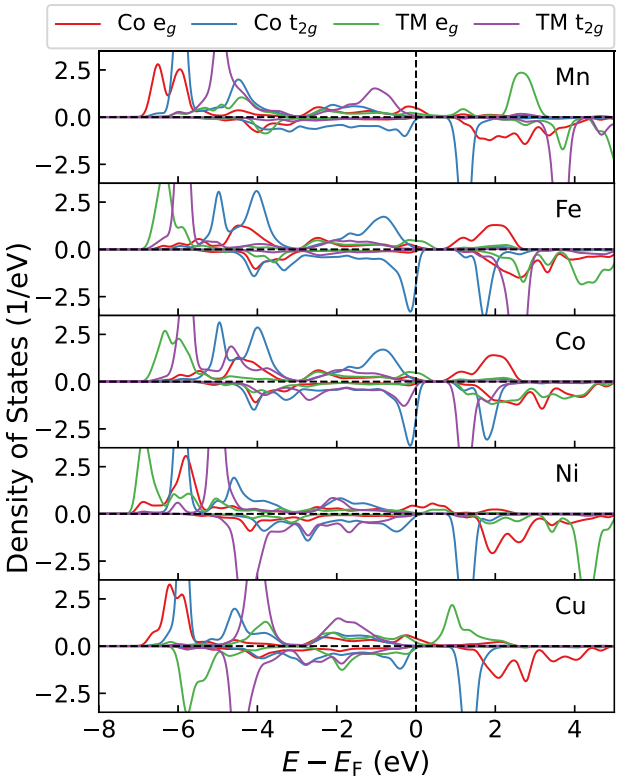


FIG. 10. The projected DOS of e_g and t_{2g} for the TM and Co 3*d* orbitals in a TM-O-Co system.

a perovskite by comparing the J value have already been reported in the literature [57,58]. To calculate effective exchange interactions, we assume a Heisenberg model for interactions between the neighboring TM ions. The calculations were performed by the TB2J package [59] based on the Green's function, and the results are presented in Table II. A minus sign is used in the exchange terms, which means a positive J value favors ferromagnetic alignment. These results qualitatively support our earlier assumption regarding orbital hybridization. Furthermore, the table presents the difference in oxygen vacancy formation energies between FM and PM states (ΔE_V^O) for each system, where the vacancy is located at the O site within the TM-O-Co bridge. Since the O ion at this site is stabilized by double exchange interactions, a larger exchange constant J correlates with a higher ΔE_V^O, as observed in the Co and Fe systems. Conversely, since superexchange does not stabilize the oxygen ion, its influence on ΔE_V^O is negligible, as demonstrated by the Cu-doped system.

TABLE II. Co-O-TM exchange coefficient (J) obtained from the DFT calculations. The formation energy shift from FM to PM (ΔE_V^O) is also shown to compare with the J.

TM	Mn	Fe	Co	Ni	Cu
J (meV)	12.5	15.3	18.1	7.7	−15.3
ΔE_V^O (eV)	0.25	0.53	0.57	0.18	−0.01

V. SUMMARY

In this study, we utilized DFT calculations to systematically explore the effects of 3*d* transition-metal doping on the oxygen vacancy formation energies in the LSC perovskite material. Two magnetic orders were considered to uncover the intricate relationships among dopant chemistry, magnetic order, and defect energetics. Our results reveal that the formation energies of oxygen vacancies in the doped LSC are strongly influenced by both the magnetic state of the system and the choice of 3*d* transition-metal dopant. The PM state, which serves as a model for general operational conditions, exhibits a different trend of oxygen vacancy formation energies when compared to the FM ground state. This difference cannot be quantitatively analyzed in terms of pristine crystal structure alteration and oxidizability of the doped elements. Utilizing the ground-state FM to assess the oxygen vacancy formation energies of a doped system may lead to qualitative inaccuracies. The reason for this inaccuracy is the effect of the doping element on the double exchange interaction, as we discussed in Fig. 10 and Table II. This emphasizes the need to account for magnetic disorder in computational studies. These findings lay the foundation for the development of customized perovskite materials with enhanced performance in electrochemical applications, such as SOFCs and oxygen separation membranes, where precise control over oxygen vacancy concentrations is paramount.

ACKNOWLEDGMENTS

This work was funded by the European Union under Grant Agreement No. 101080142, as part of the EQUALITY project. The authors thank David David (Capgemini SE) for fruitful discussions. The work was enabled in part by the Nextsim HPC at Fraunhofer ENAS.

DATA AVAILABILITY

The data that support the findings of this study are available from the corresponding author upon reasonable request.

[1] A. D. Poletayev, J. A. Dawson, M. S. Islam, and A. M. Lindenberg, Defect-driven anomalous transport in fast-ion conducting solid electrolytes, Nat. Mater. **21**, 1066 (2022).

[2] Z. Shao and S. M. Haile, A high-performance cathode for the next generation of solid-oxide fuel cells, Nature (London) **431**, 170 (2004).

[3] B. C. Steele and A. Heinzel, Materials for fuel-cell technologies, Nature (London) **414**, 345 (2001).

[4] M. Mogensen, D. Lybye, N. Bonanos, P. Hendriksen, and F. Poulsen, Factors controlling the oxide ion conductivity of fluorite and perovskite structured oxides, Solid State Ion. **174**, 279 (2004).

[5] A. Orera and P. Slater, New chemical systems for solid oxide fuel cells, Chem. Mater. **22**, 675 (2010).

[6] C. Sun, J. A. Alonso, and J. Bian, Recent advances in perovskite-type oxides for energy conversion and

storage applications, Adv. Energy Mater. **11**, 2000459 (2021).

[7] J. A. Kilner, Fast oxygen transport in acceptor doped oxides, Solid State Ion. **129**, 13 (2000).

[8] S. J. Skinner and J. A. Kilner, Oxygen ion conductors, Mater. Today **6**, 30 (2003).

[9] D. Lee, Y.-L. Lee, W. T. Hong, M. D. Biegalski, D. Morgan, and Y. Shao-Horn, Oxygen surface exchange kinetics and stability of (La, Sr)$_2$CoO$_{4\pm\delta}$/La$_{1-x}$Sr$_x$MO$_{3-\delta}$(M = Co and Fe) heterointerfaces at intermediate temperatures, J. Mater. Chem. A **3**, 2144 (2015).

[10] E. D. Wachsman and K. T. Lee, Lowering the temperature of solid oxide fuel cells, Science **334**, 935 (2011).

[11] S. B. Adler, Factors governing oxygen reduction in solid oxide fuel cell cathodes, Chem. Rev. **104**, 4791 (2004).

[12] J. Cheng, P. Ganesan, Z. Wang, M. Zhang, G. Zhang, N. Maeda, J. Matsuda, M. Yamauchi, B. Chi, and N. Nakashima, Bifunctional electrochemical properties of La$_{0.8}$Sr$_{0.2}$Co$_{0.8}$M$_{0.2}$O$_{3-\delta}$ (M = Ni, Fe, Mn, and Cu): Efficient elemental doping based on a structural and pH-dependent study, Mater. Adv. **3**, 272 (2022).

[13] D. Mantzavinos, A. Hartley, I. S. Metcalfe, and M. Sahibzada, Oxygen stoichiometries in La$_{1-x}$Sr$_x$Co$_{1-y}$Fe$_y$O$_{3-\delta}$ perovskites at reduced oxygen partial pressures, Solid State Ion. **134**, 103 (2000).

[14] S. Ingavale, M. Gopalakrishnan, C. M. Enoch, C. Pornrungroj, M. Rittiruam, S. Praserthdam, A. Somwangthanaroj, K. Nootong, R. Pornprasertsuk, and S. Kheawhom, Strategic design and insights into lanthanum and strontium perovskite oxides for oxygen reduction and oxygen evolution reactions, Small **20**, 2308443 (2024).

[15] W. Jia, Y. Wang, J. Huang, M. Li, B. Xiang, Y. Wang, L. Wu, L. Zheng, and L. Ge, Alternative B-site-doped La$_{0.6}$Sr$_{0.4}$Co$_{0.2}$Fe$_{0.8-x}$M$_x$O$_3$ (M = Ni, Cu, Nb; x = 0, 0.1, 0.2) as innovative cathode material for LT-SOFC with enhanced charge transfer and oxygen ion diffusion, Appl. Energy **353**, 122096 (2024).

[16] H. Li, Z. Su, P. Zhang, F. Liu, C. Fan, L. Xu, G. Guo, and D. Zhang, A first-principles investigation of the effects of strain and Pd-doping on ion transfer in LSCF bulk of solid oxide cells, Comput. Mater. Sci. **227**, 112276 (2023).

[17] T. Jia, J. W. Lekse, G. A. Hackett, and Y. Duan, Effects of site and magnetic disorder on the oxygen vacancy formation and electronic and optical properties of La$_x$Sr$_{1-x}$CoO$_{3-\delta}$ and SrFe$_y$Co$_{1-y}$O$_{3-\delta}$, J. Phys. Chem. C **125**, 12374 (2021).

[18] M. A. Señarís-Rodríguez and J. Goodenough, Magnetic and transport properties of the system La$_{1-x}$Sr$_x$CoO$_{3-\delta}$ ($0 \leqslant x \leqslant 0.50$), J. Solid State Chem. **118**, 323 (1995).

[19] V. Bhide, D. Rajoria, C. Rao, G. R. Rao, and V. Jadhao, Itinerant-electron ferromagnetism in La$_{1-x}$Sr$_x$CoO$_3$: A Mössbauer study, Phys. Rev. B **12**, 2832 (1975).

[20] J. Meng, N. Yuan, X. Liu, C. Yao, Q. Liang, D. Zhou, F. Meng, and J. Meng, Synergistic effects of intrinsic cation disorder and electron-deficient substitution on ion and electron conductivity in La$_{1-x}$Sr$_x$Co$_{0.5}$Mn$_{0.5}$O$_{3-\delta}$ (x = 0, 0.5, and 0.75), Inorg. Chem. **54**, 2820 (2015).

[21] M. Pavone, A. B. Munoz-Garcia, A. M. Ritzmann, and E. A. Carter, First-principles study of lanthanum strontium manganite: Insights into electronic structure and oxygen vacancy formation, J. Phys. Chem. C **118**, 13346 (2014).

[22] J. Gazquez, S. Bose, M. Sharma, M. Torija, S. Pennycook, C. Leighton, and M. Varela, Lattice mismatch accommodation via oxygen vacancy ordering in epitaxial La$_{0.5}$Sr$_{0.5}$CoO$_{3-\delta}$ thin films, APL Mater. **1**, 012105 (2013).

[23] J. Walter, G. Yu, B. Yu, A. Grutter, B. Kirby, J. Borchers, Z. Zhang, H. Zhou, T. Birol, M. Greven, and C. Leighton, Ion-gel-gating-induced oxygen vacancy formation in epitaxial La$_{0.5}$Sr$_{0.5}$CoO$_{3-\delta}$ films from in operando X-ray and neutron scattering, Phys. Rev. Mater. **1**, 071403(R) (2017).

[24] J. Woicik, C. Xie, and B. Wells, Effect of strain on the local perovskite structure: La$_{0.5}$Sr$_{0.5}$CoO$_3$, J. Appl. Phys. **109**, 083519 (2011).

[25] M. Kubicek, Z. Cai, W. Ma, B. Yildiz, H. Hutter, and J. Fleig, Tensile lattice strain accelerates oxygen surface exchange and diffusion in La$_{1-x}$Sr$_x$CoO$_{3-\delta}$ thin films, ACS Nano **7**, 3276 (2013).

[26] B. Kamecki, J. Karczewski, P. Jasiński, and S. Molin, Improvement of oxygen electrode performance of intermediate temperature solid oxide cells by spray pyrolysis deposited active layers, Adv. Mater. Interfaces **8**, 2002227 (2021).

[27] I. B. Bersuker, *The Jahn-Teller Effect* (Cambridge University Press, Cambridge, 2005).

[28] T. Mizokawa and A. Fujimori, Unrestricted Hartree-Fock study of transition-metal oxides: Spin and orbital ordering in perovskite-type lattice, Phys. Rev. B **51**, 12880 (1995).

[29] A. D. Rata, A. Herklotz, K. Nenkov, L. Schultz, and K. Dörr, Strain-induced insulator state and giant gauge factor of La$_{0.7}$Sr$_{0.3}$CoO$_3$ films, Phys. Rev. Lett. **100**, 076401 (2008).

[30] Z. Cai, Y. Kuru, J. W. Han, Y. Chen, and B. Yildiz, Surface electronic structure transitions at high temperature on perovskite oxides: The case of strained La$_{0.8}$Sr$_{0.2}$CoO$_3$ thin films, J. Am. Chem. Soc. **133**, 17696 (2011).

[31] H. Hmok, E. Martínez-Aguilar, J. Ribas-Ariño, J. S. Beltrones, J. L. S. Llamazares, and O. R. Herrera, Effect of La^{3+}/Sr^{2+} ordering on the magnetic properties of La$_{2/3}$Sr$_{1/3}$MnO$_3$ by first principles calculations, Comput. Mater. Sci. **177**, 109575 (2020).

[32] D. Louca, J. L. Sarrao, J. D. Thompson, H. Röder, and G. H. Kwei, Correlation of local Jahn-Teller distortions to the magnetic/conductive states of La$_{1-x}$Sr$_x$CoO$_3$, Phys. Rev. B **60**, 10378 (1999).

[33] A. R. Oganov, A. O. Lyakhov, and M. Valle, How evolutionary crystal structure prediction works-and why, Acc. Chem. Res. **44**, 227 (2011).

[34] See Supplemental Material at http://link.aps.org/supplemental/10.1103/6ycm-9ttt for LSC crystal structure optimization; the formation energy in 80-atom models; the convergence calculations for SCF, the force on atoms, *k*-point and energy cutoff; the stability calculations of the *U* value; the effect of spin-orbital coupling on the formation energy.

[35] D. Baskar and S. B. Adler, High temperature magnetic properties of Sr-doped lanthanum cobalt oxide (La$_{1-x}$Sr$_x$CoO$_{3-\delta}$), Chem. Mater. **20**, 2624 (2008).

[36] A. J. Thom, E. J. Sundstrom, and M. Head-Gordon, LOBA: A localized orbital bonding analysis to calculate oxidation states, with application to a model water oxidation catalyst, Phys. Chem. Chem. Phys. **11**, 11297 (2009).

[37] T. Lu, A comprehensive electron wavefunction analysis toolbox for chemists, Multiwfn, J. Chem. Phys. **161**, 082503 (2024).

[38] B. Alling, T. Marten, and I. A. Abrikosov, Effect of magnetic disorder and strong electron correlations on the thermodynamics of CrN, Phys. Rev. B **82**, 184430 (2010).

[39] M. E. Merkel, A. M. Tehrani, and C. Ederer, Probing the Mott insulating behavior of Ba_2MgReO_6 with DFT+DMFT, Phys. Rev. Res. **6**, 023233 (2024).

[40] S. Yoon, K. Jin, S. Lee, K. T. Nam, M. Kim, and Y.-K. Kwon, Effects of paramagnetic fluctuations on the thermochemistry of MnO (100) surfaces in the oxygen evolution reaction, Phys. Chem. Chem. Phys. **23**, 859 (2021).

[41] N. O. Golosova, D. P. Kozlenko, L. S. Dubrovinsky, V. Cerantola, M. Bykov, E. Bykova, S. E. Kichanov, E. V. Lukin, B. N. Savenko, A. V. Ponomareva, and I. A. Abrikosov, Magnetic and structural properties of $FeCO_3$ at high pressures, Phys. Rev. B **96**, 134405 (2017).

[42] G. Kresse and J. Furthmüller, Efficiency of *ab-initio* total energy calculations for metals and semiconductors using a plane-wave basis set, Comput. Mater. Sci. **6**, 15 (1996).

[43] P. E. Blöchl, Projector augmented-wave method, Phys. Rev. B **50**, 17953 (1994).

[44] J. P. Perdew, K. Burke, and M. Ernzerhof, Generalized gradient approximation made simple, Phys. Rev. Lett. **77**, 3865 (1996).

[45] S. L. Dudarev, G. A. Botton, S. Y. Savrasov, C. J. Humphreys, and A. P. Sutton, Electron-energy-loss spectra and the structural stability of nickel oxide: An LSDA+U study, Phys. Rev. B **57**, 1505 (1998).

[46] L. Wang, T. Maxisch, and G. Ceder, Oxidation energies of transition metal oxides within the GGA+U framework, Phys. Rev. B **73**, 195107 (2006).

[47] F. Ando, T. Gunji, T. Tanabe, I. Fukano, H. D. Abruna, J. Wu, T. Ohsaka, and F. Matsumoto, Enhancement of the oxygen reduction reaction activity of Pt by tuning its *d*-band center via transition metal oxide support interactions, ACS Catal. **11**, 9317 (2021).

[48] P. V. Balachandran and J. M. Rondinelli, Interplay of octahedral rotations and breathing distortions in charge-ordering perovskite oxides, Phys. Rev. B **88**, 054101 (2013).

[49] J. M. Rondinelli and N. A. Spaldin, Structure and properties of functional oxide thin films: Insights from electronic-structure calculations, Adv. Mater. **23**, 3363 (2011).

[50] D. Phelan, D. Louca, S. Rosenkranz, S.-H. Lee, Y. Qiu, P. J. Chupas, R. Osborn, H. Zheng, J. F. Mitchell, J. R. D. Copley, J. L. Sarrao, and Y. Moritomo, Nanomagnetic droplets and implications to orbital ordering in $La_{1-x}Sr_xCoO_3$, Phys. Rev. Lett. **96**, 027201 (2006).

[51] D. Akahoshi, M. Uchida, Y. Tomioka, T. Arima, Y. Matsui, and Y. Tokura, Random potential effect near the bicritical region in perovskite manganites as revealed by comparison with the ordered perovskite analogs, Phys. Rev. Lett. **90**, 177203 (2003).

[52] P. W. Anderson and H. Hasegawa, Considerations on double exchange, Phys. Rev. **100**, 675 (1955).

[53] O. N. Meetei, O. Erten, A. Mukherjee, M. Randeria, N. Trivedi, and P. Woodward, Theory of half-metallic double perovskites. I. Double exchange mechanism, Phys. Rev. B **87**, 165104 (2013).

[54] O. Erten, O. N. Meetei, A. Mukherjee, M. Randeria, N. Trivedi, and P. Woodward, Theory of half-metallic double perovskites. II. Effective spin Hamiltonian and disorder effects, Phys. Rev. B **87**, 165105 (2013).

[55] W. Lv, F. Krüger, and P. Phillips, Orbital ordering and unfrustrated (π, 0) magnetism from degenerate double exchange in the iron pnictides, Phys. Rev. B **82**, 045125 (2010).

[56] D. Fuchs, M. Merz, P. Nagel, R. Schneider, S. Schuppler, and H. von Löhneysen, Double exchange via t_{2g} orbitals and the Jahn-Teller effect in ferromagnetic $La_{0.7}Sr_{0.3}CoO_3$ probed by epitaxial strain, Phys. Rev. Lett. **111**, 257203 (2013).

[57] B. R. K. Nanda and S. Satpathy, Effects of strain on orbital ordering and magnetism at perovskite oxide interfaces: $LaMnO_3/SrMnO_3$, Phys. Rev. B **78**, 054427 (2008).

[58] J. Lim and J. Yu, Role of oxygen vacancy in the spin-state change and magnetic ordering in $SrCoO_{3-\delta}$, Phys. Rev. B **98**, 085106 (2018).

[59] X. He, N. Helbig, M. J. Verstraete, and E. Bousquet, TB2J: A Python package for computing magnetic interaction parameters, Comput. Phys. Commun. **264**, 107938 (2021).